

DifAttack++: Query-Efficient Black-Box Adversarial Attack via Hierarchical Disentangled Feature Space in Cross-Domain

Jun Liu, Jiantao Zhou, *Senior Member, IEEE*, Jiandian Zeng, Jinyu Tian, *Member, IEEE*, and Isao Echizen, *Senior Member, IEEE*

Abstract—This work investigates efficient score-based black-box adversarial attacks that achieve a high Attack Success Rate (ASR) and good generalization ability. We propose a novel attack framework, termed DifAttack++, which operates in a hierarchical disentangled feature space and significantly differs from existing methods that manipulate the entire feature space. Specifically, DifAttack++ firstly disentangles an image’s latent representation into an Adversarial Feature (AF) and a Visual Feature (VF) using an autoencoder equipped with a carefully designed Hierarchical Decouple-Fusion (HDF) module. In this formulation, the AF primarily governs the adversarial capability of an image, while the VF largely preserves its visual appearance. To enable the feature disentanglement and image reconstruction, we jointly train two autoencoders for the clean and adversarial image domains, i.e., cross-domain, respectively, using paired clean images and their corresponding Adversarial Examples (AEs) generated by white-box attacks on available surrogate models. During the black-box attack stage, DifAttack++ iteratively optimizes the AF based on query feedback from the victim model, while keeping the VF fixed, until a successful AE is obtained. Extensive experimental results demonstrate that DifAttack++ achieves superior ASR and query efficiency compared to state-of-the-art methods, while producing AEs with comparable visual quality. Our code is available at <https://github.com/csjunjun/DifAttackPlus.git>.

Index Terms—Black box, adversarial attack, query efficient, feature disentanglement, cross domain.

I. INTRODUCTION

Adversarial Examples (AEs) refer to images that deceive Deep Neural Networks (DNNs) by incorporating imperceptible perturbations onto clean images. Although AEs pose a security threat to many DNNs [1], it has also been observed that meticulously crafted AEs are beneficial for evaluating and improving the robustness of DNNs [2]–[5], and can even be employed for privacy protection [6]. The methods for generating AEs can be roughly classified into three categories based on the information of victim DNNs available to the

attacker. The first category is the white-box attack [7], [8], in which the attacker has access to the architecture and weights of the victim model. The second category is called the black-box attack, where the attacker can only obtain the model’s output. The case where the model’s output contains both categories and scores is known as a score-based black-box attack [9], [10], while the situation where only categories are included is named a decision-based black-box attack [11], [12]. The third category refers to the gray-box attack [13], where the attacker can obtain models’ knowledge that falls between white-box attacks and black-box attacks. Given that contemporary potent classification APIs, e.g., [14], [15], generally provide image prediction categories alongside scores, this work primarily focuses on the practical score-based black-box attacks.

We observe that State-Of-The-Art (SOTA) score-based black-box attack methods predominantly exhibit two aspects that can be improved. **On the one hand**, prior techniques that seek AEs by optimizing image features usually operate within the entire feature space, such as AdvFlow [16] and CGA [17], without embracing the disentanglement of adversarial capability and visual characteristics in the image feature. Optimizing the entire feature of images could result in substantial pixel perturbations that will encounter truncation by the predefined distortion constraint, thus diminishing the optimization efficacy of the features and eventually increasing query numbers. Another possible chain reaction is the decrease in the Attack Success Rate (ASR) caused by the limited query numbers. Although there are a few black-box methods that achieve leading ASR and query efficiency, the visual quality of their generated AEs is often unsatisfactory and quite perceptible. For instance, SquareAttack [18] usually produces AEs filled with colored stripes and squares. To improve the unsatisfactory ASR and query efficiency, meanwhile maintaining the visual quality of AEs, our DifAttack++ disentangles an image’s latent feature into an Adversarial Feature (AF) and a Visual Feature (VF), where the former dominates the adversarial capability of an image, while the latter largely determines its visual appearance. Afterward, the AF is iteratively optimized according to the query feedback, while keeping the VF unaltered.

On the other hand, some score-based attack techniques, including P-RGF [19] and GFCS [20], exploit the gradients from local white-box surrogate models to update AEs during each query. These methods are effective when image categories of the training dataset for surrogate models and the victim model are the same, namely a **close-set** black-box

J. Liu and J. Zhou are with the State Key Laboratory of Internet of Things for Smart City and the Department of Computer and Information Science, Faculty of Science and Technology, University of Macau, Macau 999078, China (e-mail: yc07453@connect.umac.mo; jtzhou@umac.mo). J. Liu is also with the Echizen Laboratory, National Institute of Informatics, Tokyo 101-8430, Japan. *Corresponding author: Jiantao Zhou.*

J. Zeng is with the Institute of Artificial Intelligence and Future Networks, Beijing Normal University, Zhuhai 519087, China (email: jian-dian@bnu.edu.cn).

J. Tian is with the School of Computer Science and Engineering, Macau University of Science and Technology, Macau 999078, China (e-mail: jy-tian@must.edu.mo).

I. Echizen is with the Echizen Laboratory, National Institute of Informatics, and University of Tokyo, Tokyo 101-8430, Japan (e-mail: ichizen@nii.ac.jp).

attack scenario analogy to the close-set recognition setting [21], [22]. When it comes to an **open-set** black-box attack, wherein the training dataset of the victim model is unknown, the effectiveness of these methods declines dramatically, as the possible incongruence between the output categories of surrogate models and the victim model hampers the calculation of gradients from surrogate models. Although there are other approaches, such as SimBA [23], CGA [17] and SquareAttack [18], which are workable in both open-set and close-set scenarios, they still face challenges in terms of the query efficiency, ASR or severe degradation of image quality. In contrast, our DifAttack++ circumvents the need to compute gradients of surrogate models when updating AEs to be queried. Instead, before embarking on querying the victim model, we leverage AEs generated by performing white-box attack methods on surrogate models to learn how to extract a disentangled AF and VF from the image’s latent feature, which enables DifAttack++ to more effectively conduct black-box attacks in open-set scenarios. The efficiency of DifAttack++ in open-set scenarios can be attributed to the fact that the disentangled feature space for optimizing AEs is also responsible for the image reconstruction task, which means that an image can still be reconstructed into its original form with a minimal loss after being mapped into our disentangled feature space. However, the feature space in other methods, such as CGA [17], is directly used to generate adversarial perturbations that are tightly bound to the data distribution of the training dataset. The latent feature for image reconstructions in DifAttack++ has better generalizability to unknown datasets than the feature space learned from adversarial perturbation distributions of a specific dataset. In addition, DifAttack++ owns the flexibility to selectively harness surrogate models, e.g., in closed-set scenarios, generating transferable AEs as the starting point for the query attack.

More specifically, in DifAttack++, we first train two distinct autoencoders equipped with the designed Hierarchical Decouple-Fusion (HDF) module to achieve image reconstructions and to disentangle AFs as well as VFs from images’ latent features. In the training stage, our proposed feature interchange operations in Cross-Domain (CD), i.e., clean and adversarial image domains, also cooperate with HDF in learning disentangled features. The feature disentanglement is feasible because the adversarial capability is mainly entwined with the decision boundary of classifiers and is relatively independent of the intrinsic image signal, whereas a contrast holds true for the visual appearance. Here, we use two autoencoders with the same architecture but different weights to extract the features of clean images and their AEs separately, since many existing works [24], [25] have pointed out that regular AEs are off the manifold of clean images. It has also been verified that the Intrinsic Dimensionality (ID) of AEs is larger than that of clean images in [26], and data with higher ID are more difficult to be modeled by DNNs [27]. Therefore, we reconstruct and disentangle clean images and AEs in CD for more precise feature representations.

After obtaining these well-trained autoencoders, in the attack stage against victim models, we iteratively optimize AFs of perturbed images using the natural evolution strategy [28],

according to the query feedback from the victim model, while keeping the VF unaltered, until a successful AE is reconstructed from the fusion of the perturbed AF and the initial VF. Specifically, the perturbed AFs are extracted from images injected with Gaussian noise. The mean of this sampling distribution is strategically initialized based on the availability of surrogate models: it is set to zero in open-set scenarios, while employing transferable adversarial perturbations in closed-set scenarios. Comprehensive details will be provided in the subsequent sections. To the best of our knowledge, this is the first work that employs the hierarchical disentangled AFs and VFs in CD for black-box adversarial attack techniques. The contributions of our work can be summarized as follows:

- We design a new hierarchical disentanglement method to distill an AF, which has a significant impact on the image’s adversarial capability while minimizing its influence on visual perception, and a VF that has the opposite attributes, from an image’s latent feature;
- Based on this disentanglement, we propose a query-efficient score-based black-box attack method, DifAttack++, which generates AEs by optimizing the AF according to query feedback while keeping the initial VF invariant;
- Experimental results demonstrate that DifAttack++ outperforms SOTA score-based black-box attack methods in ASR and query numbers simultaneously in almost all cases, meanwhile maintaining comparable visual quality of AEs, both for traditional and large-scale victim models.

Note that an earlier version of DifAttack++, called DifAttack, has been published in AAI2024 [29]. Below, we summarize their differences:

- DifAttack++ designs hierarchical convolution layers for feature disentanglement, considering that one single layer of the decouple-fusion module in DifAttack is insufficient to disentangle intensely entangled AFs and VFs;
- Compared to DifAttack, in which clean images and their AEs share the same autoencoder for the image reconstruction and feature disentanglement, the use of two cross-domain autoencoders in DifAttack++ achieves a more stable and faster training process, meanwhile leading to more effective black-box attack performance;
- DifAttack uses a clean image to start the attack in both closed-set and open-set scenarios, whereas DifAttack++ adopts a transferable AE as the starting point in closed-set scenarios to extract more powerful features, resulting in better attack efficiency;
- The ASR and query efficiency of DifAttack++ far surpass those of DifAttack, e.g., 31.5% higher ASR and 78% lower average query numbers, when performing targeted attacks on ImageNet against ResNet-101 in closed-set scenarios.

The remainder of this paper is organized as follows. Section II reviews related work. Section III presents the proposed DifAttack++ framework. Section IV reports experimental results and comparisons, and Section V concludes the paper.

II. RELATED WORKS

A. Score-based Black-box Attack Methods

Current score-based black-box attacks can be broadly categorized into two families according to whether surrogate models are used during the query-based attack stage: surrogate-free and surrogate-assisted attacks.

Surrogate-free attacks [17], [23], [29]–[32] do not exploit surrogate gradients during querying, and instead rely purely on search strategies guided by query feedback. While these methods exhibit relatively lower ASR and query efficiency, they demonstrate superior generalization in scenarios where surrogate and victim models differ in training data, particularly in open-set settings with disjoint class labels. Among them, a subset of methods, including NES [31], \mathcal{N} Attack [32], and our predecessor DifAttack [29], adopt the natural evolution strategy [28] for gradient estimation. The primary distinction among these approaches lies in the optimization space, namely the pixel space (NES), the tanh-transformed space (\mathcal{N} Attack), or a disentangled adversarial feature space (DifAttack). By operating in a low-dimensional feature space that is highly responsive to adversarial perturbations and optimization, DifAttack achieves superior ASR and query efficiency. Although CGA [17] also learns a latent distribution in advance, its Glow [33] architecture necessitates downsampling high-resolution inputs (e.g., reducing ImageNet [34] images from 224×224 to 64×64). This loss of resolution inevitably compromises its attack performance to some extent.

In contrast, surrogate-assisted attacks [10], [19], [20], [35], [36] explicitly leverage surrogate model gradients during the query phase to guide the search. For instance, methods such as P-RGF [19] and Subspace [35] bias their search directions toward surrogate gradients, while others, including BASES [36] and MCG [10], adaptively select or finetune surrogate information based on query feedback. The SOTA MCGSquare [10] further integrates the meta-learning framework of MCG with the Square [18] search strategy. Despite their effectiveness in certain settings, surrogate-assisted attacks suffer from two limitations. First, they rely on category consistency between surrogate and victim models, leading to degradations in open-set scenarios where data distributions mismatch and surrogate gradients become unreliable. Second, achieving an optimal trade-off between attack capability, query efficiency, and visual quality remains a challenge for these methods.

B. Disentangled Representation (DR)

We now give a brief introduction of DR, which aims to separate the distinct, informative generative factors of data [37]. Modern approaches often employ autoencoders [38], GANs [39], or other generative models [40] to learn this separation, frequently optimizing metrics like mutual information [41] or total correlation [42]. In the security domain, DR is most commonly harnessed for AE detection or defense [26], [43]–[45]. To our knowledge, the few attack methods involving DR are exclusively white-box approaches. For instance, RNF [46] optimizes perturbations against classifier-specific “non-robust features”, while SSAE [47] trains an autoencoder to directly generate AEs for a specific victim. These methods require

full knowledge of the victim model’s parameters to learn their respective DRs. Unlike white-box methods [46], our approach operates in black-box settings where the victim models’ parameters and architectures are completely unknown. It learns a generalizable DR from surrogate models that reconstructs the image signal itself, rather than classifier-specific features.

C. On the Distribution of Adversarial Examples

A significant body of research indicates that AEs are not mere outliers, but instead occupy a data distribution that is distinct from that of natural, clean images. Seminal works [24], [25] have demonstrated that AEs often lie “off-manifold”, residing in low-probability regions of the natural image distribution. This discrepancy is further supported by studies on ID; for example, [26] and [27] show that AEs exhibit higher ID and are more complex to model than their clean counterparts.

Despite these theoretical insights, most existing generative attack methods (e.g., CGA [17] and our predecessor DifAttack [29]) implicitly assume a shared latent manifold, employing a single generative model to represent both clean and adversarial distributions. We argue that modeling these fundamentally different distributions with a shared backbone may be sub-optimal. In contrast, DifAttack++ explicitly introduces a cross-domain architecture that respects the distinct manifold properties of clean and adversarial data.

III. PROPOSED DIFATTACK++

A. Overview

DifAttack++ aims to exploit disentangled VFs and AFs to decode AEs in score-based black-box settings, guided by query feedback from the victim model. As illustrated in Fig. 1, DifAttack++ consists of two main phases.

In the training stage, we train two U-Net-like [48] autoencoders, denoted as \mathcal{G} and \mathcal{G}^* , which share the same architecture but differ in their weights. Both autoencoders are capable of feature disentanglement and image reconstruction. Specifically, \mathcal{G} is trained on clean images \mathbf{x} , while \mathcal{G}^* is trained on their corresponding adversarial examples \mathbf{x}^* , where \mathbf{x}^* is generated by applying untargeted white-box attacks on surrogate models. Taking a clean image \mathbf{x} as an example, \mathcal{G} first disentangles its latent representation \mathbf{z} into an AF \mathbf{z}_a and a VF \mathbf{z}_v via the proposed HDF module, and then reconstructs an image $\tilde{\mathbf{x}}$ that is similar to \mathbf{x} by decoding the fused features \mathbf{z}_a and \mathbf{z}_v . Similarly, \mathcal{G}^* performs the same operations for adversarial inputs.

In the attack stage, we leverage the pre-trained autoencoders \mathcal{G} and \mathcal{G}^* to generate an adversarial example \mathbf{x}' for a given clean image \mathbf{x} against a black-box victim model \mathcal{F} . Specifically, \mathbf{x}' is obtained through an iterative optimization process. At each iteration, we sample a batch of perturbed images to extract their corresponding AFs $\hat{\mathbf{z}}_a^i$, while keeping the VF $\hat{\mathbf{z}}_v$ —which is used for subsequent image reconstruction together with $\hat{\mathbf{z}}_a^i$ —fixed and identical to that of the clean image. This procedure produces a batch of reconstructed images $\hat{\mathbf{x}}_f^i$ that are queried against \mathcal{F} . The process continues until either the query budget Q is exhausted or one of the reconstructed images $\hat{\mathbf{x}}_f^i$ successfully deceives \mathcal{F} , in which case we obtain $\mathbf{x}' = \hat{\mathbf{x}}_f^i$.

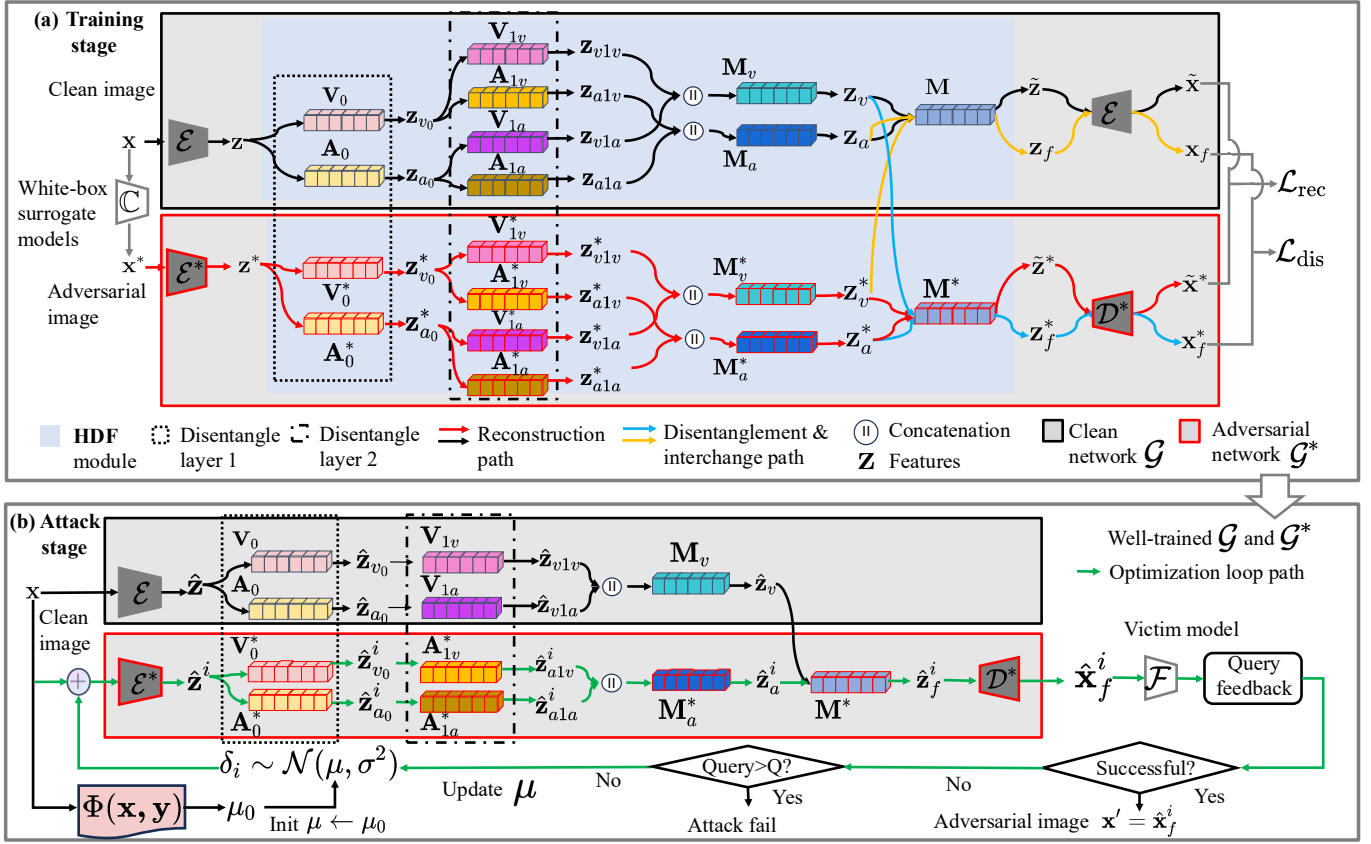


Fig. 1. (a) The training procedure of the cross-domain autoencoders \mathcal{G} and \mathcal{G}^* , equipped with the proposed HDF module to disentangle AFs (z_a) and VFs (z_v), optimized by minimizing the combined image reconstruction loss \mathcal{L}_{rec} and feature disentanglement loss \mathcal{L}_{dis} . (b) The proposed score-based black-box attack method, *DifAttack++*, which leverages the pre-trained \mathcal{G} and \mathcal{G}^* to extract VFs (\hat{z}_v) and AFs (\hat{z}_a^i), keeps the VF fixed, and iteratively optimizes the AF until a successful AE (x') is found or the query budget (Q) is exhausted.

B. Training Stage: Train Autoencoders \mathcal{G} and \mathcal{G}^*

Let x denote a clean image from the training dataset \mathbb{T} , and let \mathbb{C} represent the set of pre-trained white-box surrogate models trained on \mathbb{T} . Note that the image classes and data distribution of \mathbb{T} may differ from those of the test dataset. To generate an AE x^* corresponding to x , we adopt the white-box attack method PGD [49] by attacking a surrogate model \mathcal{C}_j , which is randomly selected from \mathbb{C} . Clearly, PGD can be replaced by other white-box attack methods, or by a combination of such methods, without significantly affecting the final attack performance of our method (see the supplementary material of *DifAttack* [29] for more details). Therefore, in this work, we adopt PGD as a representative choice. Unlike our previous work *DifAttack*, which employs a single autoencoder shared by both clean and adversarial images, we instead assign two distinct autoencoders, \mathcal{G} and \mathcal{G}^* , to the clean and adversarial domains, respectively. Notably, regular AEs usually lie off the manifold of normal images [25]. In this regard, adopting separate autoencoders is more appropriate and can lead to improved training efficiency and enhanced black-box attack performance, as will be demonstrated experimentally. In what follows, we provide a detailed description of the disentanglement and reconstruction tasks performed by the two autoencoders.

1) *Disentanglement*: To identify AFs to which an image's adversarial capability is sensitive, while ensuring that modifications to these features minimally affect visual appearance, we disentangle AFs and VFs from the image's latent representation. To this end, we exchange AFs and VFs between a clean image and its corresponding AE. The two images reconstructed from the exchanged features are then expected to exhibit adversarial capabilities and visual appearances that correspond to the images from which their respective features are derived.

HDF Module. To implement feature disentanglement, as illustrated in Fig. 1(a), we design a Hierarchical Decouple-Fusion (HDF) module. The HDF module takes an image's latent representation as input, disentangles it into VFs and AFs, and subsequently reconstructs the latent representation by fusing the disentangled features. The HDF module comprises three types of convolutional layers: visual layers (V_0, V_{1v} , and V_{1a}), adversarial layers (A_0, A_{1v} , and A_{1a}), and fusion layers (M_a, M_v , and M). All these layers are implemented as stacks of 1×1 convolutional layers. Taking a clean image x as an example, its latent representation $z = \mathcal{E}(x)$, where \mathcal{E} denotes a convolutional neural network (CNN)-based encoder, is first fed into the initial disentanglement layers V_0 and A_0 . This produces the preliminary visual features z_{v_0} and

adversarial features \mathbf{z}_{a0} , respectively:

$$\mathbf{z}_{v0} = \mathbf{V}_0(\mathbf{z}), \quad \mathbf{z}_{a0} = \mathbf{A}_0(\mathbf{z}). \quad (1)$$

Since the preliminary features \mathbf{z}_{v0} and \mathbf{z}_{a0} may still exhibit residual coupling, we further introduce a second hierarchical disentanglement stage to achieve finer-grained separation. Specifically, four additional disentanglement layers— \mathbf{V}_{1v} , \mathbf{V}_{1a} , \mathbf{A}_{1v} , and \mathbf{A}_{1a} —are appended to extract fine-grained VFs and AFs from the preliminary representations:

$$\begin{aligned} \mathbf{z}_{v1v} &= \mathbf{V}_{1v}(\mathbf{z}_{v0}), & \mathbf{z}_{v1a} &= \mathbf{V}_{1a}(\mathbf{z}_{a0}), \\ \mathbf{z}_{a1v} &= \mathbf{A}_{1v}(\mathbf{z}_{v0}), & \mathbf{z}_{a1a} &= \mathbf{A}_{1a}(\mathbf{z}_{a0}). \end{aligned} \quad (2)$$

The hierarchically calibrated visual features \mathbf{z}_{v1v} and \mathbf{z}_{v1a} are then combined through a visual fusion layer \mathbf{M}_v to produce the final disentangled visual feature \mathbf{z}_v of \mathbf{x} . Similarly, an adversarial fusion layer \mathbf{M}_a integrates \mathbf{z}_{a1v} and \mathbf{z}_{a1a} to yield the final adversarial features \mathbf{z}_a :

$$\begin{aligned} \mathbf{z}_v &= \mathbf{M}_v(\mathbf{z}_{v1v} \parallel \mathbf{z}_{v1a}), \\ \mathbf{z}_a &= \mathbf{M}_a(\mathbf{z}_{a1v} \parallel \mathbf{z}_{a1a}), \end{aligned} \quad (3)$$

where \parallel denotes channel-wise concatenation. Subsequently, \mathbf{z}_v and \mathbf{z}_a are fused through the fusion layer \mathbf{M} to reconstruct the latent representation $\tilde{\mathbf{z}}$. Overall, the feature processing of the HDF module can be summarized as

$$\mathcal{HDF}(\mathbf{z}) = \mathbf{M}(\mathbf{z}_v \parallel \mathbf{z}_a) = \tilde{\mathbf{z}}. \quad (4)$$

For clarity, we denote the HDF modules in \mathcal{G} and \mathcal{G}^* as $\mathcal{HDF}(\cdot)$ and $\mathcal{HDF}^*(\cdot)$, respectively. The corresponding fusion process in \mathcal{G}^* is defined analogously for the latent representation \mathbf{z}^* of an AE \mathbf{x}^* :

$$\mathcal{HDF}^*(\mathbf{z}^*) = \mathbf{M}^*(\mathbf{z}_v^* \parallel \mathbf{z}_a^*) = \tilde{\mathbf{z}}^*, \quad (5)$$

where \mathbf{M}^* denotes the fusion layer in \mathcal{G}^* .

Feature Interchange in CD. With the HDF module in place, we now describe how feature interchange is performed in the cross-domain (CD) to facilitate effective disentanglement. Specifically, as illustrated by the yellow path in Fig. 1(a), the AFs of a clean image \mathbf{z}_a are concatenated with the VFs of an adversarial image \mathbf{z}_v^* , and the resulting features are fed into the fusion layer \mathbf{M} to obtain a fused representation \mathbf{z}_f . Symmetrically, as shown by the blue path in Fig. 1(a), another fused representation \mathbf{z}_f^* is obtained by combining the VFs of the clean image \mathbf{z}_v with the AFs of the adversarial image \mathbf{z}_a^* :

$$\mathbf{z}_f = \mathbf{M}(\mathbf{z}_v^* \parallel \mathbf{z}_a), \quad \mathbf{z}_f^* = \mathbf{M}(\mathbf{z}_v \parallel \mathbf{z}_a^*). \quad (6)$$

Given the fused features, the corresponding reconstructed images \mathbf{x}_f and \mathbf{x}_f^* are then obtained as

$$\mathbf{x}_f = \mathcal{D}(\mathbf{z}_f), \quad \mathbf{x}_f^* = \mathcal{D}^*(\mathbf{z}_f^*), \quad (7)$$

where \mathcal{D} and \mathcal{D}^* denote the CNN-based decoders in \mathcal{G} and \mathcal{G}^* , respectively.

Disentanglement Loss. Subsequently, to enforce that AFs primarily govern the adversarial capability of an image, while VFs mainly determine its perceptual appearance, we impose complementary constraints on the reconstructed images. Specifically, the fused image \mathbf{x}_f is expected to be visually similar to the adversarial example \mathbf{x}^* while remaining

non-adversarial. In contrast, \mathbf{x}_f^* should preserve the visual appearance of the clean image \mathbf{x} , yet remain adversarial against all surrogate models to enhance the generalization of AFs across different classifiers. Accordingly, we define the disentanglement loss L_{dis} as

$$\begin{aligned} L_{dis} &= \|\mathbf{x}^* - \mathbf{x}_f\|_2 + \frac{1}{N} \sum_{j=1}^N L_{adv}(\mathbf{x}_f, y, 1, \mathcal{C}_j, k) \\ &+ \|\mathbf{x} - \mathbf{x}_f^*\|_2 + \frac{1}{N} \sum_{j=1}^N L_{adv}(\mathbf{x}_f^*, y, 0, \mathcal{C}_j, k), \end{aligned} \quad (8)$$

where N denotes the cardinality of the surrogate model set \mathcal{C} . The ℓ_2 norm measures the Euclidean distance between two images, and L_{adv} quantifies adversarial effectiveness. Following [50], we employ the margin loss for optimization. Unlike cross-entropy, this formulation allows us to explicitly control the attack confidence k . This loss is formulated as:

$$\begin{aligned} L_{adv}(\mathbf{x}, y, v, \mathcal{C}_j, k) &= \\ \max \left\{ \mathbb{I}(v) \cdot (\mathcal{C}_j(\mathbf{x}, y) - \max_{h \neq y} \mathcal{C}_j(\mathbf{x}, h)), -k \right\}. \end{aligned} \quad (9)$$

Here, $v \in \{0, 1\}$ specifies the attack type. Specifically, $\mathbb{I}(0) = 1$ corresponds to an untargeted attack with ground-truth label y , whereas $\mathbb{I}(1) = -1$ indicates a targeted attack with target class y . Moreover, $\mathcal{C}_j(\mathbf{x}, h)$ denotes the output score of classifier \mathcal{C}_j for class h .

2) *Reconstruction:* To enforce cycle consistency [51] in the context of feature disentanglement, as illustrated by the reconstruction paths in Fig. 1(a), the autoencoder is required to reconstruct an input image well even after its latent representation has been processed by the HDF module. Accordingly, the outputs of the HDF modules, denoted as $\tilde{\mathbf{z}}$ and $\tilde{\mathbf{z}}^*$, are expected to reconstruct images $\tilde{\mathbf{x}} \approx \mathbf{x}$ and $\tilde{\mathbf{x}}^* \approx \mathbf{x}^*$, respectively, via

$$\tilde{\mathbf{x}} = \mathcal{D}(\mathcal{HDF}(\mathbf{z})), \quad \tilde{\mathbf{x}}^* = \mathcal{D}^*(\mathcal{HDF}^*(\mathbf{z}^*)). \quad (10)$$

Based on these reconstructions, we define the reconstruction loss L_{rec} for networks \mathcal{G} and \mathcal{G}^* as

$$L_{rec} = \|\mathbf{x} - \tilde{\mathbf{x}}\|_2 + \|\mathbf{x}^* - \tilde{\mathbf{x}}^*\|_2. \quad (11)$$

Finally, the overall objective optimized during the training of \mathcal{G} and \mathcal{G}^* is given by

$$L_{all} = \lambda \cdot L_{rec} + L_{dis}, \quad (12)$$

where the hyperparameter λ controls the trade-off between the reconstruction and disentanglement losses.

C. Attack Stage: Generating the AE \mathbf{x}'

VF. After obtaining the well-trained models \mathcal{G} and \mathcal{G}^* , we leverage them in the attack stage to generate AEs under a black-box setting. As illustrated in Fig. 1(b), given a clean image \mathbf{x} , our goal is to attack the victim model \mathcal{F} while preserving the visual fidelity of the generated adversarial image. To this end, we keep the VF used for decoding the perturbed image $\hat{\mathbf{x}}_f^i$ identical to that of the original image \mathbf{x} . Specifically, the VF $\hat{\mathbf{z}}_v$ is extracted as

$$\begin{aligned} \hat{\mathbf{z}} &= \mathcal{E}(\mathbf{x}), \\ \hat{\mathbf{z}}_{v0} &= \mathbf{V}_0(\hat{\mathbf{z}}), \quad \hat{\mathbf{z}}_{a0} = \mathbf{A}_0(\hat{\mathbf{z}}), \\ \hat{\mathbf{z}}_{v1v} &= \mathbf{V}_{1v}(\hat{\mathbf{z}}_{v0}), \quad \hat{\mathbf{z}}_{v1a} = \mathbf{V}_{1a}(\hat{\mathbf{z}}_{a0}), \\ \hat{\mathbf{z}}_v &= \mathbf{M}_v(\hat{\mathbf{z}}_{v1v} \parallel \hat{\mathbf{z}}_{v1a}). \end{aligned} \quad (13)$$

This design encourages $\hat{\mathbf{x}}_f^i$ to remain as close as possible to the clean image in terms of perceptual appearance.

AF. With the VF fixed, the next objective is to identify an AF $\hat{\mathbf{z}}_a^i$ such that, when combined with $\hat{\mathbf{z}}_v$, it can successfully deceive the victim model \mathcal{F} . For instance, in the untargeted attack setting, we aim to generate an adversarial image $\hat{\mathbf{x}}_f^i$ by solving

$$\begin{aligned} \hat{\mathbf{x}}_f^i &= \mathcal{D}^*(\mathbf{M}^*(\hat{\mathbf{z}}_v \parallel \hat{\mathbf{z}}_a^i)), \\ \text{s.t. } \arg \max_h \mathcal{F}(\hat{\mathbf{x}}_f^i, h) &\neq y, \quad \|\hat{\mathbf{x}}_f^i - \mathbf{x}\|_p \leq \epsilon, \end{aligned} \quad (14)$$

where y denotes the ground-truth label of \mathbf{x} . For targeted attacks, the first constraint is modified to $\arg \max_h \mathcal{F}(\hat{\mathbf{x}}_f^i, h) = y$, where y now represents the target class.

To obtain a suitable AF \mathbf{z}_a^i , we search for a perturbation δ_i in the pixel space such that the resulting perturbed image $\mathbf{x} + \delta_i$ induces adversarially effective AFs. This design choice is motivated by the fact that the pixel space allows more direct and precise control over the perturbation magnitude than the feature space. To alleviate the curse of dimensionality and exploit local gradient similarity [52], the optimization is conducted in a downsampled pixel space $\mathbb{R}^{C \times (H/s) \times (W/s)}$ with scaling factor s . Formally, $\hat{\mathbf{z}}_a^i$ is extracted as

$$\begin{aligned} \hat{\mathbf{z}}^i &= \mathcal{E}^*(\mathbf{x} + \text{up}(\delta_i, s)), \\ \hat{\mathbf{z}}_{v0}^i &= \mathbf{V}_0^*(\hat{\mathbf{z}}^i), \quad \hat{\mathbf{z}}_{a0}^i = \mathbf{A}_0^*(\hat{\mathbf{z}}^i), \\ \hat{\mathbf{z}}_{a1v}^i &= \mathbf{A}_{1v}^*(\hat{\mathbf{z}}_{v0}^i), \quad \hat{\mathbf{z}}_{a1a}^i = \mathbf{A}_{1a}^*(\hat{\mathbf{z}}_{a0}^i), \\ \hat{\mathbf{z}}_a^i &= \mathbf{M}_a^*(\hat{\mathbf{z}}_{a1v}^i \parallel \hat{\mathbf{z}}_{a1a}^i), \end{aligned} \quad (15)$$

where $\text{up}(\cdot)$ denotes the upsampling operation that projects δ_i back to the original input resolution. The candidate adversarial image is then reconstructed as

$$\hat{\mathbf{x}}_f^i = \Pi_{\epsilon, \mathbf{x}}(\mathcal{D}^*(\mathbf{M}^*(\hat{\mathbf{z}}_v \parallel \hat{\mathbf{z}}_a^i))), \quad (16)$$

where $\hat{\mathbf{z}}_v$ is fixed as defined in Eq. (13), and $\hat{\mathbf{z}}_a^i$ is iteratively optimized through Eq. (15) by updating δ_i . The operator $\Pi_{\epsilon, \mathbf{x}}$ projects the image onto the ℓ_p -ball of radius ϵ centered at \mathbf{x} , ensuring that the perturbation satisfies the prescribed constraint. For simplicity, we denote the right-hand side of Eq. (16) as $\mathbf{T}(\mathbf{x} + \text{up}(\delta_i))$.

By combining Eq. (16) with a change-of-variables formulation, we unify the attack objective in Eq. (14) as

$$\begin{aligned} \min_{\boldsymbol{\mu}} \mathbb{E}_{\mathcal{N}(\boldsymbol{\mu}, \sigma^2)} L_{adv}(\mathbf{T}(\mathbf{x} + \text{up}(\delta_i)), y, v, \mathcal{F}, k), \\ \text{s.t. } \|\mathbf{T}(\mathbf{x} + \text{up}(\delta_i)) - \mathbf{x}\| \leq \epsilon, \end{aligned} \quad (17)$$

where $\hat{\mathbf{x}}_f^i = \mathbf{T}(\hat{\mathbf{x}} + \text{up}(\delta_i))$ satisfies the untargeted or targeted attack condition accordingly. We sample δ_i from a Gaussian distribution $\mathcal{N}(\boldsymbol{\mu}, \sigma^2)$, where the mean $\boldsymbol{\mu}$ is optimized and the variance σ is fixed based on a grid search. To optimize $\boldsymbol{\mu}$, we adopt the natural evolution strategy [28] to estimate the gradient of the expected adversarial loss with respect to $\boldsymbol{\mu}$. Using stochastic gradient descent with learning rate η and batch size τ , the update rule is

$$\boldsymbol{\mu} \leftarrow \boldsymbol{\mu} - \frac{\eta}{\tau \sigma} \sum_{i=1}^{\tau} \gamma_i L_{adv}(\mathbf{T}(\mathbf{x} + \text{up}(\boldsymbol{\mu} + \sigma \gamma_i)), y, v, \mathcal{F}, k), \quad (18)$$

where $\gamma_i \sim \mathcal{N}(\mathbf{0}, I)$. Once a feasible solution for $\boldsymbol{\mu}$ is obtained, a successful AE \mathbf{x}' can be sampled as

$$\mathbf{x}' = \hat{\mathbf{x}}_f^i = \mathbf{T}(\mathbf{x} + \text{up}(\boldsymbol{\mu} + \sigma \gamma_i)). \quad (19)$$

However, the convergence and effectiveness of this optimization heavily depend on the initialization of $\boldsymbol{\mu}$. Poor initialization often leads to slow convergence or failure to satisfy the perturbation constraint. To address this, we design two tailored initialization strategies for open-set and closed-set scenarios, denoted as **Dif++_{open}** and **Dif++_{close}**, respectively. In open-set settings, due to the uncertainty of class categories, surrogate models often produce predictions inconsistent with the victim model, leading to unreliable transferability. In closed-set settings, we instead exploit adversarial transferability by introducing an adversarially biased initialization. The initialization can be unified as

$$\boldsymbol{\mu}_0 = \begin{cases} \mathbf{0}, & \text{open-set,} \\ \text{down}(\mathcal{A}(\mathbf{x}, y, \mathbb{C}, \epsilon), s), & \text{closed-set,} \end{cases} \quad (20)$$

which we denote as $\Phi(\mathbf{x}, y)$. Here, $\text{down}(\cdot)$ denotes a down-sampling operator with scale s , and \mathcal{A} represents an adversarial attack algorithm that, given a clean image \mathbf{x} , its label y , a set of surrogate models \mathbb{C} , and a perturbation budget ϵ , produces a perturbed image within the allowed budget. We instantiate \mathcal{A} using PGN [53] for untargeted attacks and FTM [54] for targeted attacks due to their strong transferability. \mathcal{A} is flexible and can be replaced with stronger methods in the future.

Zero-Shot AE Check. Prior to the iterative optimization of $\boldsymbol{\mu}$, we conduct a preliminary verification to exploit the high adversarial sensitivity of the disentangled AF space. Specifically, we generate a candidate AE via Eq. (16) and query the victim model. If this initial candidate successfully misleads the model, the attack terminates immediately, thereby significantly reducing query costs. Otherwise, we proceed to the iterative optimization of $\boldsymbol{\mu}$ as formulated in Eqs. (17)-(18). This mechanism effectively enables a potential ‘‘zero-shot’’ attack. The complete workflow is summarized in Algorithm 1, with this verification step detailed in Lines 3-7. Additionally, following [32], we normalize the adversarial loss L_{adv} (Line 20) to stabilize convergence.

IV. EXPERIMENTS

In this section, we conduct a comprehensive evaluation of DifAttack++ against SOTA score-based black-box attack methods. The experiments encompass both *closed-set* and *open-set* scenarios, and further extend to real-world commercial APIs and defensive mechanisms. In addition, we analyze the adversarial sensitivity of the disentangled features and visualize their impact on image reconstruction. Finally, ablation studies are conducted to validate the contributions of the cross-domain architecture, the HDF module, and the initialization strategies.

A. Experiment Setup

1) *Datasets:* For closed-set scenarios, we utilize the large-scale *ImageNet-1k* [34], hereafter referred to as ImageNet, as both the training and test dataset. Images are cropped and

TABLE I

RESULTS OF SCORE-BASED BLACK-BOX ATTACKS ON IMAGENET FOR THE “simple group”. THE ATTACK SUCCESS RATE (ASR, %) AS WELL AS THE AVERAGE AND MEDIAN NUMBERS OF QUERIES (AVG.Q/MED.Q) ARE REPORTED AS EVALUATION METRICS. THE BEST AND SECOND-BEST RESULTS ARE HIGHLIGHTED IN **BOLD** AND UNDERLINED, RESPECTIVELY.

Scenarios	Victims	GoogleNet				VGG16				ResNet18				SqueezeNet											
		Targeted		Untargeted		Targeted		Untargeted		Targeted		Untargeted		Targeted		Untargeted									
		ASR	Avg.Q	Med.Q	ASR	Avg.Q	Med.Q	ASR	Avg.Q	Med.Q	ASR	Avg.Q	Med.Q	ASR	Avg.Q	Med.Q	ASR	Avg.Q	Med.Q						
Query w/o surrogate	SignH	28.1	9,021	10,000	<u>95.5</u>	1,504	452	60.8	7,606	8,401	100.0	702	194	49.8	7,935	9,950	<u>99.5</u>	931	212	45.7	8,315	10,000	100.0	363	11
	NES	37.7	8,748	10,000	100.0	1,234	682	47.7	8,328	10,000	98.0	1,068	605	54.3	7,988	9,242	97.5	1,264	682	45.7	8,235	10,000	91.0	1,711	589
	\mathcal{N} Attack	76.9	6,883	7,323	100.0	878	606	93.5	5,924	5,858	100.0	752	505	94.5	5,324	5,101	100.0	780	606	90.0	5,644	5,202	100.0	563	404
	SimBA	77.5	5,874	5,489	100.0	865	419	<u>97.5</u>	3,505	3,016	99.0	533	269	97.0	3,873	3,445	<u>99.5</u>	614	361	94.0	4,230	3,620	<u>99.5</u>	428	252
	CGA	90.9	4,645	-	100.0	<u>139</u>	-	91.1	4,801	-	99.4	137	-	91.6	4,222	-	97.3	475	-	93.2	3,972	-	99.3	202	-
	DifAttack	97.0	3,173	2,625	100.0	165	40	100.0	2,246	2,018	100.0	<u>123</u>	54	100.0	1,901	1,793	100.0	156	64	98.0	2,793	2,775	100.0	91	8
	Dif++ _{open}	98.5	2,678	2,241	100.0	111	21	100.0	1,348	1,133	100.0	44	1	100.0	1,351	1,189	100.0	81	6	99.0	2,085	1,796	100.0	40	1
Query w/ surrogate	BASES	12.5	8,901	10,000	81.7	2,080	1	26.7	8,229	10,000	95.5	564	69	15.4	9,228	10,000	85.1	1,717	1	35.3	7,179	10,000	86.4	1,549	1
	P-RGF	60.2	5,222	4,588	93.0	1,162	157	58.3	6,093	7,043	98.0	529	85	51.3	6,393	9,601	96.0	711	70	65.3	5,433	4,995	95.0	796	119
	Subspace	50.3	6,642	9,874	95.5	994	40	68.3	4,964	3,984	95.5	867	31	66.3	4,750	3,034	94.5	917	28	33.2	8,063	10,000	97.0	566	25
	GFCs	60.0	6,359	7,101	<u>96.5</u>	1,348	463	93.0	3,358	2,494	100.0	515	107	95.0	3,274	2,744	100.0	739	229	72.5	6,127	3,161	98.5	658	128
	MCGSquare	96.0	2,937	2,132	100.0	174	14	100.0	1,816	1,568	100.0	49	1	99.5	1,346	1,073	100.0	61	1	99.0	1,633	1,323	100.0	37	1
	Dif++ _{close}	99.5	1,020	541	100.0	19	1	100.0	432	229	100.0	11	1	100.0	573	369	100.0	20	1	99.5	859	506	100.0	27	1

TABLE II

RESULTS OF SCORE-BASED BLACK-BOX ATTACKS ON IMAGENET FOR THE “complex group”.

Scenarios	Victims	Swin-V2-T				EfficientNet-B3				ResNet101				ConvNeXtBase											
		Targeted		Untargeted		Targeted		Untargeted		Targeted		Untargeted		Targeted		Untargeted									
		ASR	Avg.Q	Med.Q	ASR	Avg.Q	Med.Q	ASR	Avg.Q	Med.Q	ASR	Avg.Q	Med.Q	ASR	Avg.Q	Med.Q	ASR	Avg.Q	Med.Q						
Query w/o surrogate	SignH	44.2	8,212	10,000	82.9	3,049	968	31.7	8,847	10,000	87.4	2,611	677	6.5	9,744	10,000	66.3	4,670	3,544	20.6	9,216	10,000	81.9	3,979	2,950
	NES	30.7	8,722	10,000	95.0	2,093	1,122	15.6	9,382	10,000	95.5	2,185	1,199	10.6	9,606	10,000	90.0	3,013	1,913	11.1	9,471	10,000	86.4	3,561	2,499
	\mathcal{N} Attack	66.8	7,473	7,979	99.0	1,298	808	32.2	8,825	10,000	99.0	1,390	808	20.6	9,128	10,000	96.5	1,888	1,263	40.7	8,609	10,000	100.0	2,012	1,465
	SimBA	84.0	5,822	4,064	98.5	2,185	990	65.0	7,585	6,242	98.0	1,419	584	30.5	8,618	10,000	73.0	3,581	739	90.0	4,809	4,249	98.5	1,065	406
	DifAttack	92.0	4,291	3,729	100.0	409	171	69.0	6,080	5,709	100.0	400	151	62.5	6,680	6,954	99.0	523	149	97.0	3,850	3,461	100.0	435	231
	Dif++ _{open}	95.0	3,516	2,611	100.0	170	57	87.5	4,833	4,276	100.0	302	129	69.0	6,419	4,674	99.0	447	103	100.0	1,706	1,456	100.0	149	1
	Query w/ surrogate	P-RGF	62.3	4,610	2,264	96.5	755	66	49.3	6,244	10,000	90.0	1,345	66	34.7	7,256	10,000	89.5	1,301	82	57.3	5,720	7,090	88.9	1,381
Subspace		61.3	6,597	7,252	99.0	882	138	55.3	6,834	8,757	95.5	993	121	35.7	7,978	10,000	95.5	1,198	136	76.9	5,206	4,297	99.0	569	135
GFCs		61.5	5,683	5,479	86.5	1,794	12	57.0	5,897	5,233	89.0	1,692	345	36.0	7,577	10,000	87.0	1,521	14	71.0	4,270	2,690	91.5	1,621	44
MCGSquare		99.0	2,352	1,934	100.0	251	72	95.0	3,738	3,255	99.5	463	64	75.5	6,079	6,104	99.5	400	15	100.0	2,762	2,429	100.0	226	53
Dif++ _{close}		100.0	294	91	100.0	60	1	95.5	1,669	795	100.0	138	1	94.0	1,460	226	99.5	172	1	100.0	705	421	100.0	83	1

resized to 224×224 to match standard classifier inputs. For open-set scenarios, the training dataset remains ImageNet, whereas the test datasets differ and include *Food101* [55], which contains 101 fine-grained food categories, and *ObjectNet* [56], consisting of natural images with complex rotations, backgrounds, and viewpoints. Images are resized to 224×224 for Food101 and 336×336 for ObjectNet. Notably, when attacking ObjectNet, we exclude 131 classes that overlap with ImageNet to ensure a strictly open-set evaluation, following the protocol in [56].

2) *Victim and Surrogate Models*: We select a diverse suite of models to serve as victims and surrogates, categorized according to their architectures and training paradigms.

Standard ImageNet Classifiers. We collect eight pre-trained models with diverse architectures from Torchvision library [57]. Since the official source code for ImageNet in the baseline method CGA [17] is unavailable, we evaluate our method on the same models used in CGA (ResNet18, VGG16, GoogleNet, and SqueezeNet) and report their official results for fair comparison. In addition, we conduct further experiments on higher-performance models, including ConvNeXtBase, EfficientNet-B3, Swin-V2-T, and ResNet101. Based on their clean classification accuracy on ImageNet, we partition these models into two groups: a “simple” group (clean accuracy $< 80\%$) and a “complex” group (clean accuracy $\geq 80\%$). Following the protocol in CGA, we adopt a “leave-one-out” strategy within each group, where three models are used as surrogates to guide the attack against the remaining fourth victim model.

Foundation Models. To further verify the efficacy against large-scale pre-training, and considering the pivotal role of CLIP in large vision-language models [58]–[61], we target OpenAI’s CLIP models [62], including ViT-B/16 (trained on Web Image-Text pairs) and ViT-H-14-CLIPA-336 (trained on the DataComp-1B [63] dataset). These models serve as victim classifiers in open-set evaluations on the Food101 and ObjectNet datasets.

Real-world API & Defenses. We also extend our evaluation to the commercial Imagga API [15], as well as to a range of defensive mechanisms. The specific configurations and settings for these targets are detailed in the corresponding subsections.

3) *Comparative Methods*: For a fair comparison, based on the reliance on surrogate models during the attack stage, we divide the comparative methods into two groups: 1) *surrogate-free* methods, including SignH [30], NES [31], \mathcal{N} Attack [32], SimBA [23], CGA [17], DifAttack [29], and our proposed **Dif++_{open}** (which initializes the AF from clean images); and 2) *surrogate-assisted* methods, including BASES [36], P-RGF [19], Subspace [35], GFCs [20], MCGSquare (a combination of MCG [10] and Square [18], representing the SOTA in ASR and query efficiency), as well as our **Dif++_{close}** (which initializes the AF from the image augmented with transferable perturbations).

4) *Implementation Details*: Consistent with the baselines, the maximum perturbation budget is set to $\epsilon = 12/255$ under the l_∞ norm, while the maximum query budget is set to 10,000 for offline models. For the real-world Imagga API, the query budget is further restricted to 500 in order to reflect

Algorithm 1 DifAttack++

Input: Target classifier \mathcal{F} ; clean image \mathbf{x} ; query budget Q ; perturbation budget ϵ ; ground-truth/target label y (for untargeted/targeted attacks); learning rate η ; variance σ ; parameters v and k in Eq. (17); sample size τ ; downsampling/upsampling factor s .

Output: Adversarial image \mathbf{x}' .

```

1: Initialize query counter  $q \leftarrow 1$ 
2: Initialize  $\mu_0 \leftarrow \mathbf{0}$  for open-set scenarios (Dif++open),
   or set  $\mu_0$  via Eq. (20) for close-set scenarios (Dif++close)
3: Sample initial mean  $\mu \sim \mathcal{N}(\mu_0, I)$ 
4: Generate an initial adversarial candidate  $\hat{\mathbf{x}}_f^0$  using Eq. (16)
5: if  $L_{adv}(\hat{\mathbf{x}}_f^0, y, v, \mathcal{F}, k) = -k$  then
6:   return  $\mathbf{x}' \leftarrow \hat{\mathbf{x}}_f^0$ 
7: end if
8: while  $q + \tau \leq Q$  do
9:   Sample  $\gamma_1, \dots, \gamma_\tau \sim \mathcal{N}(\mathbf{0}, I)$ 
10:  Set  $\delta_i \leftarrow \mu + \sigma \gamma_i, \forall i \in \{1, \dots, \tau\}$ 
11:  Compute adversarial candidates  $\hat{\mathbf{x}}_f^i$  using Eqs. (13), (15), and (16)
12:  Evaluate  $l_i \leftarrow L_{adv}(\hat{\mathbf{x}}_f^i, y, v, \mathcal{F}, k), \forall i$ 
13:  Update query count  $q \leftarrow q + \tau$ 
14:  if  $\exists i$  s.t.  $l_i = -k$  then
15:    return  $\mathbf{x}' \leftarrow \hat{\mathbf{x}}_f^i$ 
16:    break
17:  else
18:    Normalize losses  $\hat{l}_i \leftarrow (l_i - \text{mean}(\{l_i\}))/\text{std}(\{l_i\}), \forall i$ 
19:    Update mean  $\mu \leftarrow \mu - \frac{\eta}{\tau\sigma} \sum_{i=1}^{\tau} \hat{l}_i \gamma_i$ 
20:  end if
21: end while
22: return  $\mathbf{x}'$ 

```

practical cost constraints. Regarding the hyperparameters of DifAttack++, we set the sampling variance $\sigma = 0.1$, the downscaling factor $s = 4$, the learning rate $\eta = 0.01$, and the margin constant $\kappa = 5$. All experiments are conducted on NVIDIA GeForce RTX 3090 GPUs.

B. Performance in Closed-Set Scenarios

In closed-set scenarios, the attacker has access to surrogate models trained on the same dataset as the victim model, making both surrogate-free and surrogate-assisted methods applicable. Therefore, we report the performance of both types of methods under this setting. Tables I and II summarize the results in terms of Attack Success Rate (ASR), as well as the average and median number of queries (Avg.Q and Med.Q), for victim models in the “simple group” and “complex group”, respectively. Across extensive experimental settings, both variants of DifAttack++, namely Dif++_{close} and Dif++_{open}, consistently achieves higher ASR and substantially lower query costs than their respective baselines, while producing AEs with improved or at least comparable perceptual quality (see Fig. 2).

Effectiveness of Zero-Shot AE Check. In untargeted attacks, Dif++_{close} achieves a Med.Q of 1 across almost all victim models while maintaining equal or higher ASR. Achieving Med.Q= 1 indicates that the AE generated by our zero-shot AE check already succeeds in over half of the cases, before any iterative query refinement. In contrast, the runner-up method MCGSquare attains Med.Q= 1 only on victim models in the simple group; when attacking complex architectures, its Med.Q rises sharply—typically exceeding 50. These results demonstrate that our disentangled attack mechanism remains

highly effective even against strong and modern architectures, and that the zero-shot adversarial feature decoupling plays a dominant role in early attack success.

Targeted Attacks. In the more challenging targeted setting, Dif++_{close} maintains a clear performance lead in both effectiveness and efficiency. For example, when attacking ResNet101, our method improves ASR by 18.5% over MCGSquare while simultaneously reducing the Med.Q by 96%. This substantial reduction in query cost highlights the practical efficiency of the proposed disentangled optimization strategy under challenging targeted constraints.

Generalization Across Architectures. DifAttack++ maintains a stable performance advantage even when the surrogate and victim models belong to substantially different architectural families—such as CNNs (e.g., ResNet, EfficientNet), hierarchical vision transformers (e.g., Swin-V2-T), and modern convolutional backbones inspired by transformers (e.g., ConvNeXt). This result confirms that our cross-domain disentanglement framework captures generalized adversarial features that are robust to architectural discrepancies, rather than merely overfitting to surrogate-specific gradients.

Superiority of Dif++_{open}. Furthermore, even in the absence of surrogate models, Dif++_{open} outperforms most surrogate-assisted baselines in terms of both ASR and query efficiency. Notably, it achieves a query efficiency gain of up to 38.2% compared to MCGSquare in targeted attacks against ConvNeXtBase. This superiority is consistently observed in targeted attack scenarios on GoogleNet, VGG16, ResNet18, and ConvNeXtBase, as well as in untargeted attack scenarios on GoogleNet, VGG16, Swin-V2-T, EfficientNet-B3, and ConvNeXtBase. Compared with the vanilla DifAttack, Dif++_{open} demonstrates substantial performance improvements, which further validates the effectiveness of our proposed decoupling mechanism and refined attack strategy. The individual contributions of these modules are elaborated in the subsequent ablation studies.

C. Performance in Open-Set Scenarios

In this subsection, we evaluate the attack performance under the more challenging open-set scenarios. This setup tests the generalization capability of attack methods under domain shifts. For these experiments, we employ methods from the surrogate-free group.

CLIP. Table III presents the comparative results against CLIP models. It is shown that Dif++_{open} achieves significant improvements in both ASR and query efficiency compared to the baseline methods. Notably, on the ObjectNet dataset, our method demonstrates remarkable robustness. For instance, in targeted attacks, Dif++_{open} outperforms DifAttack by over 11% in ASR. These results verify that our cross-domain disentanglement strategy learns general AFs that transcend specific domains. Even without prior knowledge of the target domain, optimizing in our disentangled adversarial latent space yields substantially better performance than optimizing in the pixel space (as in NES) or in a tanh-transformed pixel space (as in \mathcal{N} Attack), despite all three methods relying on the same natural evolution strategy.

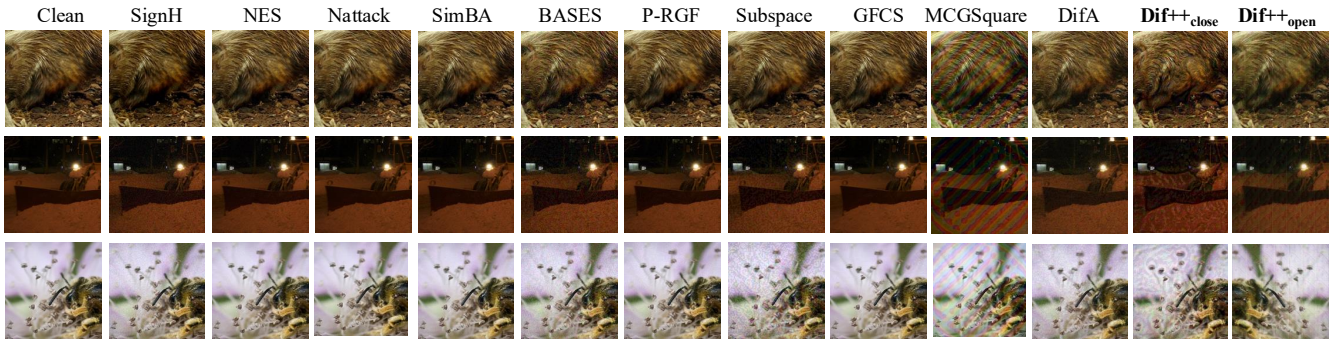


Fig. 2. Visualization of AEs generated by SOTA score-based attack methods. Our methods yield visually more imperceptible AEs than the corresponding runner-up approaches in both surrogate-assisted (Dif++_{close} vs. MCGSquare) and surrogate-free (Dif++_{open} vs. DifAttack (DifA)) settings.

TABLE III

RESULTS OF SURROGATE-FREE SCORE-BASED BLACK-BOX ATTACKS AGAINST CLIP MODELS IN OPEN-SET SCENARIOS.

Datasets	Settings Methods	Targeted			Untargeted		
		ASR	Avg.Q	Med.Q	ASR	Avg.Q	Med.Q
Food101	SimBA	69.7	5,929	5,416	97.5	1,392	816
	SignH	<u>84.0</u>	4,545	3,551	<u>99.0</u>	745	261
	Nattack	51.0	6,990	9,588	100.0	312	255
	NES	29.5	8,278	10,000	100.0	609	496
	DifAttack	<u>84.0</u>	3,717	2,371	100.0	<u>100</u>	<u>41</u>
	Dif++ _{open}	90.0	2,942	1,466	100.0	59	31
	ObjectNet	SimBA	18.0	9,210	10,000	60.0	5,474
SignH		<u>49.5</u>	7,166	10,000	90.6	2,012	423
Nattack		36.0	7,585	10,000	100.0	556	217
NES		22.0	8,597	10,000	<u>99.5</u>	1,550	1,550
DifAttack		46.5	6,693	10,000	100.0	270	11
Dif++ _{open}		57.5	5,825	5,551	100.0	204	<u>21</u>

TABLE IV

RESULTS OF SURROGATE-FREE SCORE-BASED BLACK-BOX ATTACKS AGAINST REAL-WORLD IMAGGA API IN OPEN-SET SCENARIOS.

Settings→ Methods↓	Untargeted			Targeted		
	ASR	Avg.Q	Med.Q	ASR	Avg.Q	Med.Q
SignH	70.0	186	<u>14</u>	63.6	212	10
Nattack	76.7	192	31	38.2	406	61
SimBA	60.0	292	364	54.5	244	261
DifAttack	<u>80.0</u>	<u>132</u>	25	<u>68.2</u>	197	30
Dif++ _{open}	86.7	92	6	72.7	163	<u>21</u>

Real-World API. To further assess practical applicability, we conduct attacks against the commercial Imagga API [15]. This API employs a recognition model trained on a massive and undisclosed dataset covering over 3,000 categories, thereby representing a true “black-box” setting with unknown training data. Due to API call limitations, we compare against several top-performing open-set methods, including DifAttack, SimBA, NAttack, and SignH. For untargeted attacks, the objective is to remove the top-3 predicted classes, whereas for targeted attacks, we aim to promote the second-highest scoring class to the top rank. As shown in Table IV, Dif++_{open} consistently dominates in this real-world scenario. Despite the complete lack of knowledge regarding the API’s training distribution, our method reliably achieves higher ASR with fewer queries. In particular, for targeted attacks, our approach significantly reduces the query cost compared to query-intensive methods such as SimBA and NAttack. These results indicate that the proposed disentangled feature space remains effective even in a large-scale and unknown label space. Overall, this experiment strongly underscores the practical utility and cost-effectiveness of DifAttack++ for evaluating the robustness of commercial AI services.

D. Robustness against Defensive Mechanisms

To verify the resilience of the generated AEs, we evaluate the performance of DifAttack++ against SOTA defensive

strategies. These defenses can be broadly categorized into two types: model-level defenses, such as Adversarial Training (AT) [64], and input-level purification methods, including Bit-depth Reduction (Bit-Red) [65], Neural Representation Purifier (NRP) [66], and Diffusion Purifier (DiffPure) [67]. For the AT defense, following the protocol in CGA [17], we employ an adversarially trained ResNet-50 as the surrogate model. Subsequently, all methods are evaluated by generating AEs to attack a more robust, adversarially trained Wide-ResNet-50-2 victim model. In contrast, for input purification defenses, we generate AEs targeting a standard ResNet-18 model on ImageNet. These AEs are then passed through the corresponding purification modules before being classified by the victim model.

The comparative results in Table V clearly demonstrate the superior robustness of our method. DifAttack++ achieves the highest average ASR across all four defensive techniques and under both attack settings (query with or without surrogate models). Notably, Dif++_{close} surpasses the runner-up method, MCGSquare, by a substantial margin of 9% in terms of the averaged ASR across different defensive techniques. Specifically, the resilience to input-level purification techniques suggests that our cross-domain fusion strategy effectively embeds adversarial features into the semantic structure of the image. In contrast to pixel-level noise, which can be easily smoothed out, the disentangled adversarial features fused by our HDF module are more integral to the image representation, and thus difficult to purify without compromising visual fidelity. Furthermore, the success against the AT-protected victim model further confirms that our disentanglement mechanism is capable of extracting robust and generalized adversarial features even from robust surrogate models, thereby validating the overall efficacy of the proposed framework.

E. Analysis on Disentangled Features

To verify the disentanglement efficacy of DifAttack++ and to elucidate the distinct roles of VF and AF, we conduct both quantitative sensitivity analyses and qualitative visualization experiments on ImageNet.

Quantitative Analysis on Adversarial Sensitivity. We first examine the impact of perturbing specific features on attack performance. Specifically, we perform an ablation study in which Gaussian noise with varying standard deviation ξ is injected exclusively into either VFs or AFs of clean images, extracted via the single-encoder in DifAttack (baseline) or the cross-domain autoencoders in DifAttack++, while keeping the counterpart feature fixed. The reconstructed images are then evaluated across eight diverse classifiers. As evidenced by the results illustrated in Fig. 3, the AF extracted by the autoencoder \mathcal{G}^* in DifAttack++ (AF++) exhibits markedly superior adversarial sensitivity. In particular, the ASR curve of AF++ (red line) behaves like a step function, saturating to nearly 100% almost immediately, even under negligible perturbation (e.g., $\xi = 0.001$). In sharp contrast, the baseline AF (orange line) shows a much slower, sigmoid-like increase, requiring significantly larger perturbation magnitudes to achieve comparable success. Conversely, perturbing the VF (blue and green lines) leads to much smaller changes in ASR, which confirms that the VF is largely decoupled from adversarial effectiveness. In a few cases (e.g., Figs. 3 (g) and (h)), the ASR of AF++ marginally lags behind that of AF at high perturbation levels ($\xi > 0.05$). However, this discrepancy is of limited practical relevance. Since pixel-domain distortion is not clipped in this sensitivity analysis, such relatively large ξ values typically exceed the predefined perturbation constraint in practice. As a result, perturbations with $\xi < 0.05$ are more meaningful for guiding our attack method. Consequently, the primary indicator of effectiveness lies in the low-perturbation regime, where AF++ demonstrates clear and consistent dominance.

Qualitative Analysis on Semantic Information. To further visualize the semantic information encoded in VFs and AFs, we perform a cross-instance feature swapping experiment. Given two clean images \mathbf{x}_1 and \mathbf{x}_2 , we extract their disentangled features $\{\mathbf{z}_v, \mathbf{z}_a\}$ using the pre-trained clean autoencoder and synthesize mixed images by swapping feature components: $\tilde{\mathbf{x}}_{v1a2} = \mathcal{D}(\mathcal{HDF}(\mathbf{M}(\mathbf{z}_{v1}||\mathbf{z}_{a2})))$ and $\tilde{\mathbf{x}}_{v2a1} = \mathcal{D}(\mathcal{HDF}(\mathbf{M}(\mathbf{z}_{v2}||\mathbf{z}_{a1})))$. As shown in Fig. 4, the visual appearance of the reconstructed images is predominantly governed by the VF. Specifically, $\tilde{\mathbf{x}}_{v1a2}$ preserves the structural identity and texture of \mathbf{x}_1 regardless of the injected foreign AF \mathbf{z}_{a2} , confirming that our framework effectively isolates benign visual semantics within the VF. This is further supported by the progressive fusion results in Fig. 5: linearly interpolating the VF transitions the visual content from one object (e.g., bee) to another (e.g., bed), whereas varying the AF yields almost no perceptible visual changes.

Furthermore, the role of AFs becomes more evident through an analysis of the residual maps between the self-reconstructed image and the swapped image (e.g., $\tilde{\mathbf{x}}_1 - \tilde{\mathbf{x}}_{v1a2}$). As shown in the last two columns of Fig. 4, these residuals are not random

TABLE V
RESULTS OF COMPARATIVE METHODS AGAINST VARIOUS SOTA DEFENSIVE TECHNIQUES ON IMAGENET IN UNTARGETED SETTINGS.

Scenarios	Methods	AT	BitRed	NRP	DiffPure	Avg.ASR
Query w/o surrogate	SignH	36.7	38.0	28.9	12.6	29.1
	NES	18.6	21.0	31.3	20.0	22.7
	\mathcal{N} -Attack	39.2	45.0	34.9	24.0	35.8
	SimBA	39.5	14.5	37.2	13.1	26.0
	DifAttack	<u>52.5</u>	<u>46.5</u>	<u>41.5</u>	<u>28.5</u>	<u>42.3</u>
	Dif++ _{open}	64.5	88.8	45.4	40.4	43.7
Query w/ surrogate	BASES	0.0	58.5	32.6	8.6	24.9
	P-RGF	43.2	38.0	<u>38.5</u>	30.4	37.5
	Subspace	54.8	54.0	31.2	14.8	38.7
	GFCs	6.8	21.5	32.9	22.5	20.9
	MCGSquare	<u>70.5</u>	<u>72.0</u>	34.5	<u>65.5</u>	<u>60.0</u>
	Dif++ _{close}	71.0	92.0	43.5	69.5	69.0

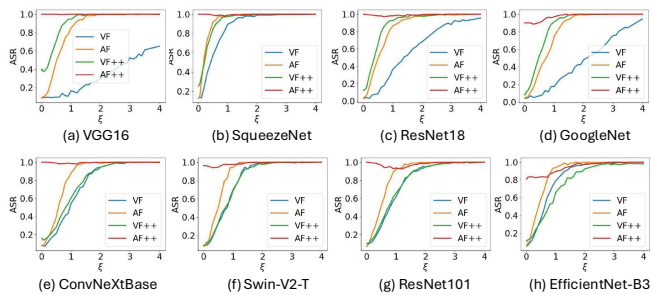


Fig. 3. Adversarial sensitivity of clean images’ VF and AF from DifAttack, or VF++ and AF++ from DifAttack++. The x-axis starts at 0.001. Higher ASR values indicate greater adversarial sensitivity.

TABLE VI
ABLATION STUDY OF THE CROSS-DOMAIN AUTOENCODERS (CD), THE HDF MODULE, AND THE TRANSFERABLE INITIALIZATION (TI) ON THE VICTIM MODEL CONVNEXTBASE.

CD	HDF	TI	Targeted			Untargeted		
			ASR	Avg.Q	Med.Q	ASR	Avg.Q	Med.Q
			97	3,850	3,461	100	435	231
✓			100	1,669	1,411	100	189	11
✓	✓		100	1,706	1,456	100	149	1
✓	✓	✓	100	705	421	100	83	1

noise; rather, they emerge as spatially localized activation maps that closely align with foreground objects. For example, in the first row, the residual concentrates precisely on the “black stork”, while in the second row, it highlights the “dining table”. This phenomenon suggests that the AF captures the classifier’s attention regions and encodes high-level, class-discriminative cues that are largely independent of background texture. Consequently, when the original AF is replaced with a foreign one, the primary changes occur in these sensitive semantic regions, effectively “rewriting” the features used for classification without altering the human-perceptible structure of the image.

F. Ablation Studies

To substantiate the contribution of each proposed component, we conduct the ablation study starting from the baseline (original DifAttack). We investigate three key enhancements: 1) the Cross-Domain (CD) training scheme, 2) the Hierarchical

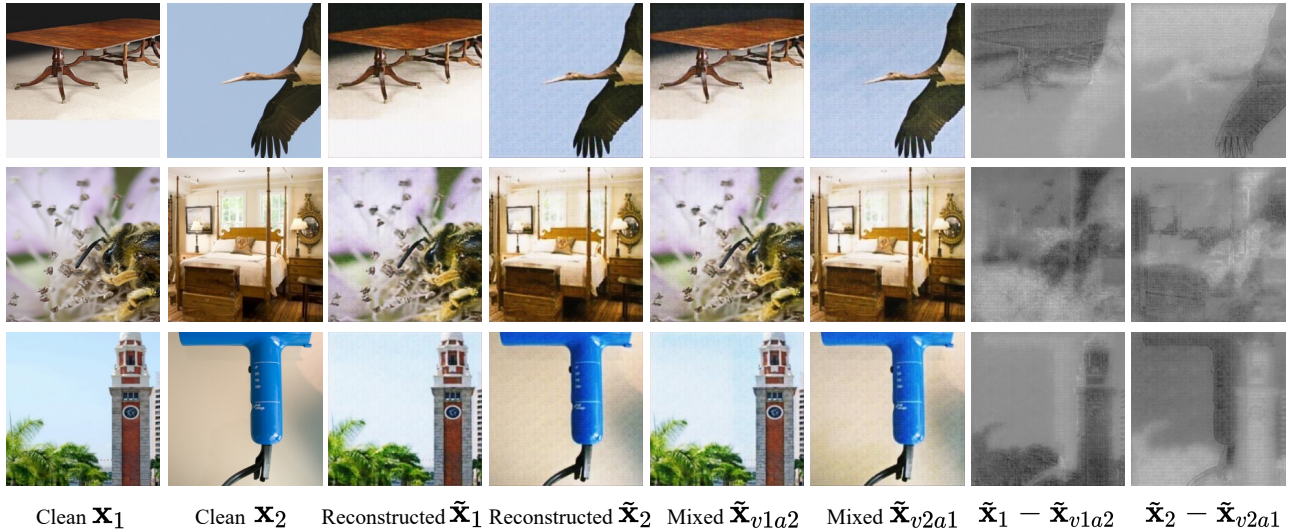


Fig. 4. Visualization of clean images’ disentangled representations extracted by the autoencoder \mathcal{G} in DifAttack++. Reconstructed images show that visual appearance is dominated by the VF, whereas swapping the AF induces localized semantic changes concentrated on foreground objects, revealing that AF captures class-discriminative attention regions while remaining visually imperceptible.

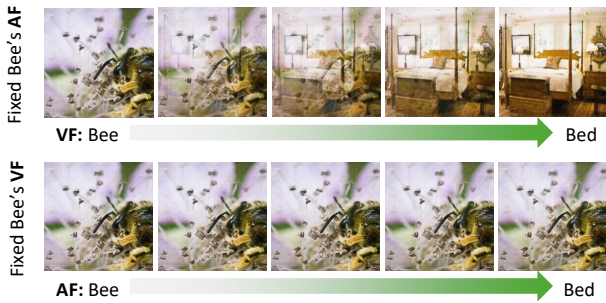


Fig. 5. Progressive fusion of clean images’ disentangled features extracted by the autoencoder \mathcal{G} in DifAttack++. Increasing VFs’ contribution induces a gradual visual transition between images, whereas modifying AFs with fixed VFs produces negligible perceptual changes, highlighting the distinct roles of VFs and AFs.

Decouple-Fusion (**HDF**) module, and 3) the Transferable Initialization (**TI**) strategy. The quantitative results are summarized in Table VI.

CD. Replacing the single shared autoencoder with the cross-domain architecture yields significant performance gains. As shown in the third row of Table VI, it improves both ASR and query efficiency across the board. Notably, in the challenging targeted attack scenario, CD not only boosts ASR by 3% but also delivers a remarkable 56.6% improvement in query efficiency, providing a solid foundation for the framework.

HDF. The transition from a single-layer DF to the two-layer HDF module has a profound impact on untargeted attacks, slashing the Med.Q to 1. This confirms that deeper, hierarchical decoupling extracts purer adversarial features, enabling successful zero-shot random perturbation directly from the latent space. However, we observe a slight performance dip in targeted attacks. We attribute this to the increased complexity of HDF, which may overfit the specific decision boundaries of the surrogate models used during training. Unlike untargeted

attacks that merely require crossing the local boundary, targeted attacks necessitate precise navigation to a specific remote decision region [54]. This makes them inherently more sensitive to the boundary mismatch between surrogate and victim models. This finding highlights a critical trade-off between the depth of disentanglement and generalization, marking a pivotal direction for future research.

TI. Finally, integrating the adversarial biased VF acts as a powerful “warm start” for the optimization. When applied on top of the CD and HDF, it propels the search into a high-potential subspace, further and dramatically enhancing both ASR and query efficiency.

G. Impact of Cross-Domain Architecture

A critical question is whether the performance gains of DifAttack++ stems from the proposed cross-domain disentanglement mechanism or simply from the increased model capacity (i.e., doubled parameters compared to the single-encoder baseline). To isolate the source of improvement, we conduct a comparative study focusing on model capacity and optimization dynamics.

Specifically, we construct two parameter-equivalent variants of the single-autoencoder baseline (denoted as **1 AE**, ~ 12.8 MB): 1) **Deep-AE**: Increasing the network depth by stacking convolutional layers. 2) **Wide-AE**: Expanding the channel dimensions of the encoder/decoder. Both variants match the parameter budget (~ 25.8 MB) of our cross-domain framework (**2 AEs** without HDF module). We track two critical metrics during training to evaluate the quality of the learned representations: self-reconstruction Loss (\mathcal{L}_{rec}), which measures the capability of the autoencoders to faithfully reconstruct images within their respective domains, and the averaged adversarial loss \mathcal{L}_{adv} of the feature-exchanged AEs $\tilde{\mathbf{x}}^* = \mathcal{D}^*(\mathcal{HDF}^*(\mathbf{M}^*(\mathbf{z}_v || \mathbf{z}_a^*)))$. The comparative trajectories are plotted in Fig. 6. As observed in the reconstruction loss

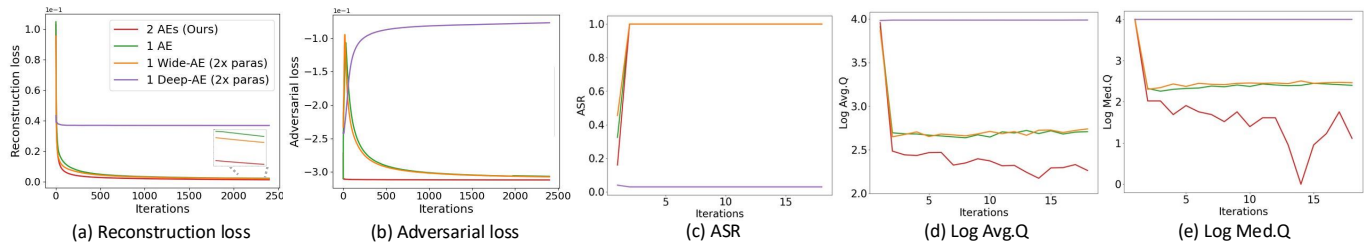


Fig. 6. Comparison of training dynamics and attack performance under equivalent parameter budgets. The cross-domain architecture (Red) consistently outperforms parameter-matched baselines (Wide/Deep-AE) in minimizing reconstruction/adversarial losses (Left) and maximizing attack efficiency (Right). Note: The x-axis values differ slightly between loss and attack metrics due to different checkpoint recording intervals.

curve in Fig. 6(a), the cross-domain architecture (red curve) achieves the fastest convergence and the lowest final loss compared to all single-autoencoder variants (Wide/Deep/1-AE). This indicates that by physically isolating clean and adversarial domains, our framework enables each encoder-decoder pair to specialize in its respective domain, leading to more accurate reconstruction without requiring excessive model depth or width.

Furthermore, the adversarial loss curve in Fig. 6(b) demonstrates the effectiveness of our disentanglement strategy. This metric quantifies how “adversarial” the synthesized image appears when an AF is injected into a clean VF: the lower the value, the stronger the adversarial capability. Our method (red curve) starts from a significantly lower initial value and consistently outperforms the baselines, confirming that the disentangled representation successfully preserves adversarial semantics during synthesis. This advantage also translates into improved query efficiency. As shown in Figs. 6(c–d), the cross-domain architecture achieves a substantially lower query cost from the early stages of optimization. In contrast, the Wide-AE performs comparably to the baseline, suggesting that merely increasing model capacity cannot alleviate the feature entanglement bottleneck. The Deep-AE exhibits suboptimal and unstable convergence, likely due to gradient vanishing or explosion in deeper networks lacking specialized designs such as residual connections. Together, these results demonstrate that simply scaling up model capacity—via width (Wide-AE) or depth (Deep-AE)—yields only marginal or unstable improvements. The significant performance gain of DifAttack++ thus stems not from increased parameters, but from the structural advantage of cross-domain disentanglement.

V. CONCLUSION

This work presents a novel query-efficient score-based black-box adversarial attack method named DifAttack++, which aims to hierarchically disentangle the AFs and VFs from an image’s latent feature and perform black-box attacks via the disentangled feature space in cross-domain. The main idea is to optimize the AF while keeping the VF unchanged until a successful AE is obtained. Experimental results demonstrate the superior attack efficiency of DifAttack++ in both close-set and open-set scenarios, meanwhile maintaining a satisfactory visual quality of AEs.

REFERENCES

- [1] X. Du, X. Liu, J. Zhou, Z. Lin, C.-m. Pun, C. Wu, T. Li, Z. Chen, W. Ni, and J. Luo, “Defensive Adversarial CAPTCHA: A Semantics-Driven Framework for Natural Adversarial Example Generation,” *IEEE Trans. Dependable Secure Comput.*, vol. 23, no. 02, pp. 3423–3435, 2026.
- [2] F. Croce and M. Hein, “Reliable evaluation of adversarial robustness with an ensemble of diverse parameter-free attacks,” in *Proc. Int. Conf. Mach. Learn.*, 2020, pp. 2206–2216.
- [3] F. Li, K. Li, H. Wu, J. Tian, and J. Zhou, “Toward robust learning via core feature-aware adversarial training,” *IEEE Trans. Inf. Forensics Secur.*, vol. 20, pp. 6236–6251, 2025.
- [4] —, “Dat: Improving adversarial robustness via generative amplitude mix-up in frequency domain,” in *Proc. Adv. Neural Inf. Process. Syst.*, vol. 37, 2024, pp. 127 099–127 128.
- [5] H. Wang, R. Sun, C. Chen, M. Xue, L.-K. Soon, S. Wang, and Z. Jin, “Iterative window mean filter: Thwarting diffusion-based adversarial purification,” *IEEE Trans. Dependable Secure Comput.*, vol. 22, no. 2, pp. 1827–1844, 2024.
- [6] J. Liu, J. Zhou, J. Tian, and W. Sun, “Recoverable privacy-preserving image classification through noise-like adversarial examples,” *ACM Trans. Multimedia Comput. Commun. Appl.*, vol. 20, no. 7, may 2024.
- [7] H. Zhang, Y. Avrithis, T. Furon, and L. Amsaleg, “Walking on the edge: Fast, low-distortion adversarial examples,” *IEEE Trans. Inf. Forensics Secur.*, vol. 16, pp. 701–713, 2021.
- [8] Y. Wang, C. Zhang, H. Zhou, Z. Ying, Z. Xiong, W. Zhou, and L. Zhu, “Boosting Adversarial Transferability of Vision Transformers,” *IEEE Trans. Dependable Secure Comput.*, vol. 23, no. 01, pp. 329–342, 2026.
- [9] R. Liu, W. Zhou, T. Zhang, K. Chen, J. Zhao, and K.-Y. Lam, “Boosting black-box attack to deep neural networks with conditional diffusion models,” *IEEE Trans. on Inf. Forensics and Secur.*, vol. 19, pp. 5207–5219, 2024.
- [10] F. Yin, Y. Zhang, B. Wu, Y. Feng, J. Zhang, Y. Fan, and Y. Yang, “Generalizable black-box adversarial attack with meta learning,” *IEEE Trans. Pattern Anal. Mach. Intell.*, vol. 46, no. 3, p. 1804–1818, Mar. 2024.
- [11] Z. Zhao, Z. Li, F. Zhang, Z. Yang, S. Luo, T. Li, R. Zhang, and K. Ren, “Sage: steering the adversarial generation of examples with accelerations,” *IEEE Trans. on Inf. Forensics and Secur.*, vol. 18, pp. 789–803, 2023.
- [12] Z. Chen, B. Li, S. Wu, S. Ding, and W. Zhang, “Query-efficient decision-based black-box patch attack,” *IEEE Trans. on Inf. Forensics and Secur.*, vol. 18, pp. 5522–5536, 2023.
- [13] G. Apruzzese and V. S. Subrahmanian, “Mitigating Adversarial Gray-Box Attacks Against Phishing Detectors,” *IEEE Trans. Dependable Secure Comput.*, vol. 20, no. 05, pp. 3753–3769, 2023.
- [14] Google, “Google cloud vision api,” “<https://cloud.google.com/vision>”, 2024, accessed:2024-06-07.
- [15] Imagga, “Ai-powered image tagging api,” “<https://imagga.com/solutions/auto-tagging>”, 2024, accessed:2024-06-07.
- [16] H. Mohaghegh Dolatabadi, S. Erfani, and C. Leckie, “Advflow: Inconspicuous black-box adversarial attacks using normalizing flows,” in *Proc. Adv. Neural Inf. Process. Syst.*, 2020, pp. 15 871–15 884.
- [17] Y. Feng, B. Wu, Y. Fan, L. Liu, Z. Li, and S.-T. Xia, “Boosting black-box attack with partially transferred conditional adversarial distribution,” in *Proc. IEEE Conf. Comput. Vis. Pattern Recognit.*, 2022, pp. 15 095–15 104.
- [18] M. Andriushchenko, F. Croce, N. Flammarion, and M. Hein, “Square attack: a query-efficient black-box adversarial attack via random search,” in *Proc. Eur. Conf. Comput. Vis.* Springer, 2020, pp. 484–501.

- [19] S. Cheng, Y. Dong, T. Pang, H. Su, and J. Zhu, "Improving black-box adversarial attacks with a transfer-based prior," in *Proc. Adv. Neural Inf. Process. Syst.*, vol. 32, 2019.
- [20] N. A. Lord, R. Mueller, and L. Bertinetto, "Attacking deep networks with surrogate-based adversarial black-box methods is easy," in *Proc. Int. Conf. Learn. Represent.*, 2022.
- [21] S. Vaze, K. Han, A. Vedaldi, and A. Zisserman, "Open-set recognition: A good closed-set classifier is all you need," in *Proc. Int. Conf. Learn. Represent.*, 2021.
- [22] H. Wu, J. Zhou, X. Zhang, J. Tian, and W. Sun, "Robust camera model identification over online social network shared images via multi-scenario learning," *IEEE Trans. Inf. Forensics Secur.*, vol. 19, pp. 148–162, 2023.
- [23] C. Guo, J. Gardner, Y. You, A. G. Wilson, and K. Weinberger, "Simple black-box adversarial attacks," in *Proc. Int. Conf. Mach. Learn.*, 2019, pp. 2484–2493.
- [24] D. Stutz, M. Hein, and B. Schiele, "Disentangling adversarial robustness and generalization," in *Proc. IEEE Conf. Comput. Vis. Pattern Recognit.*, 2019, pp. 6976–6987.
- [25] W.-A. Lin, C. P. Lau, A. Levine, R. Chellappa, and S. Feizi, "Dual manifold adversarial robustness: Defense against lp and non-lp adversarial attacks," in *Proc. Adv. Neural Inf. Process. Syst.*, vol. 33, 2020, pp. 3487–3498.
- [26] Y. Qing, T. Bai, Z. Liu, P. Moulin, and B. Wen, "Detection of adversarial attacks via disentangling natural images and perturbations," *IEEE Trans. Inf. Forensics Secur.*, vol. 19, pp. 2814–2825, 2024.
- [27] P. Pope, C. Zhu, A. Abdelkader, M. Goldblum, and T. Goldstein, "The intrinsic dimension of images and its impact on learning," in *Proc. Int. Conf. Learn. Represent.*, 2020.
- [28] D. Wierstra, T. Schaul, T. Glasmachers, Y. Sun, J. Peters, and J. Schmidhuber, "Natural evolution strategies," *J. Mach. Learn. Res.*, vol. 15, no. 1, pp. 949–980, 2014.
- [29] J. Liu, J. Zhou, J. Zeng, and J. Tian, "Difattack: Query-efficient black-box attack via disentangled feature space," in *Proc. AAAI Conf. Artif. Intell.*, vol. 38, no. 4, Mar. 2024, pp. 3666–3674.
- [30] A. Al-Dujaili and U.-M. O'Reilly, "Sign bits are all you need for black-box attacks," in *Proc. Int. Conf. Learn. Represent.*, 2020.
- [31] A. Ilyas, L. Engstrom, A. Athalye, and J. Lin, "Black-box adversarial attacks with limited queries and information," in *Proc. Int. Conf. Mach. Learn.*, 2018, pp. 2137–2146.
- [32] Y. Li, L. Li, L. Wang, T. Zhang, and B. Gong, "Nattack: Learning the distributions of adversarial examples for an improved black-box attack on deep neural networks," in *Proc. Int. Conf. Mach. Learn.*, 2019, pp. 3866–3876.
- [33] Y. Lu and B. Huang, "Structured output learning with conditional generative flows," in *Proc. AAAI Conf. Artif. Intell.*, vol. 34, no. 04, 2020, pp. 5005–5012.
- [34] J. Deng, W. Dong, R. Socher, L.-J. Li, K. Li, and L. Fei-Fei, "Imagenet: A large-scale hierarchical image database," in *Proc. IEEE Conf. Comput. Vis. Pattern Recognit.*, IEEE, 2009, pp. 248–255.
- [35] Y. Guo, Z. Yan, and C. Zhang, "Subspace attack: Exploiting promising subspaces for query-efficient black-box attacks," in *Proc. Adv. Neural Inf. Process. Syst.*, vol. 32, 2019.
- [36] Z. Cai, C. Song, S. Krishnamurthy, A. Roy-Chowdhury, and S. Asif, "Blackbox attacks via surrogate ensemble search," in *Proc. Adv. Neural Inf. Process. Syst.*, vol. 35, 2022, pp. 5348–5362.
- [37] Y. Bengio, A. Courville, and P. Vincent, "Representation learning: A review and new perspectives," *IEEE Trans. Pattern Anal. Mach. Intell.*, vol. 35, no. 8, pp. 1798–1828, 2013.
- [38] H.-Y. Lee, H.-Y. Tseng, Q. Mao, J.-B. Huang, Y.-D. Lu, M. K. Singh, and M.-H. Yang, "Drit++: Diverse image-to-image translation via disentangled representations," *Int. J. Comput. Vis.*, pp. 1–16, 2020.
- [39] C. Meo, L. Mahon, A. Goyal, and J. Dauwels, "atc-vae: On the relationship between disentanglement and diversity," in *Proc. Int. Conf. Learn. Represent.*, 2024.
- [40] X. Ma, X. Kong, S. Zhang, and E. H. Hovy, "Decoupling global and local representations via invertible generative flows," in *Proc. Int. Conf. Learn. Represent.*, 2020.
- [41] C. P. Burgess, I. Higgins, A. Pal, L. Matthey, N. Watters, G. Desjardins, and A. Lerchner, "Understanding disentangling in beta-VAE," *arXiv preprint arXiv:1804.03599*, 2018.
- [42] H. Kim and A. Mnih, "Disentangling by factorising," in *Proc. Int. Conf. Mach. Learn.*, 2018, pp. 2649–2658.
- [43] A. Mustafa, S. H. Khan, M. Hayat, R. Goecke, J. Shen, and L. Shao, "Deeply supervised discriminative learning for adversarial defense," *IEEE Trans. Pattern Anal. Mach. Intell.*, vol. 43, no. 9, pp. 3154–3166, 2020.
- [44] S. Wang, S. Nepal, C. Rudolph, M. Grobler, S. Chen, T. Chen, and Z. An, "Defending adversarial attacks via semantic feature manipulation," *IEEE Trans. Serv. Comput.*, vol. 15, no. 6, pp. 3184–3197, 2021.
- [45] S. Yang, T. Guo, Y. Wang, and C. Xu, "Adversarial robustness through disentangled representations," in *Proc. AAAI Conf. Artif. Intell.*, vol. 35, no. 4, 2021, pp. 3145–3153.
- [46] J. Kim, B.-K. Lee, and Y. M. Ro, "Distilling robust and non-robust features in adversarial examples by information bottleneck," in *Proc. Adv. Neural Inf. Process. Syst.*, vol. 34, 2021, pp. 17148–17159.
- [47] S. Lu, Y. Xian, K. Yan, Y. Hu, X. Sun, X. Guo, F. Huang, and W.-S. Zheng, "Discriminator-free generative adversarial attack," in *Proc. ACM Int. Conf. Multimedia.*, 2021, pp. 1544–1552.
- [48] O. Ronneberger, P. Fischer, and T. Brox, "U-net: Convolutional networks for biomedical image segmentation," in *International Conference on Medical image computing and computer-assisted intervention*. Springer, 2015, pp. 234–241.
- [49] A. Madry, A. Makelov, L. Schmidt, D. Tsipras, and A. Vladu, "Towards deep learning models resistant to adversarial attacks," in *Proc. Int. Conf. Learn. Represent.*, 2018.
- [50] N. Carlini and D. Wagner, "Towards evaluating the robustness of neural networks," in *Proc. IEEE Symp. Secur. Priv.*, 2017, pp. 39–57.
- [51] J.-Y. Zhu, T. Park, P. Isola, and A. A. Efros, "Unpaired image-to-image translation using cycle-consistent adversarial networks," in *Proc. IEEE Conf. Comput. Vis.*, 2017.
- [52] A. Ilyas, L. Engstrom, and A. Madry, "Prior convictions: Black-box adversarial attacks with bandits and priors," in *Proc. Int. Conf. on Learn. Represent.*, 2019.
- [53] Z. Ge, H. Liu, W. Xiaosen, F. Shang, and Y. Liu, "Boosting adversarial transferability by achieving flat local maxima," *Proc. Adv. Neural Inf. Process. Syst.*, vol. 36, pp. 70141–70161, 2023.
- [54] K. Liang, X. Dai, Y. Li, D. Wang, and B. Xiao, "Improving transferable targeted attacks with feature tuning mixup," in *Proc. IEEE Conf. Comput. Vis. Pattern Recognit.*, 2025, pp. 25802–25811.
- [55] L. Bossard, M. Guillaumin, and L. Van Gool, "Food-101—mining discriminative components with random forests," in *Proc. Eur. Conf. Comput. Vis.*. Springer, 2014, pp. 446–461.
- [56] A. Barbu, D. Mayo, J. Alverio, W. Luo, C. Wang, D. Gutfreund, J. Tenenbaum, and B. Katz, "Objectnet: A large-scale bias-controlled dataset for pushing the limits of object recognition models," in *Proc. Adv. Neural Inf. Process. Syst.*, vol. 32, 2019.
- [57] PyTorch, <https://github.com/pytorch/vision>, 2023.
- [58] Y. Zhang, A. Unell, X. Wang, D. Ghosh, Y. Su, L. Schmidt, and S. Yeung-Levy, "Why are visually-grounded language models bad at image classification?" *Proc. Adv. Neural Inf. Process. Syst.*, vol. 37, pp. 51727–51753, 2024.
- [59] D. Zhang, Y. Yu, J. Dong, C. Li, D. Su, C. Chu, and D. Yu, "Mm-llms: Recent advances in multimodal large language models," in *Find. Assoc. Comput. Linguist.*, 2024, pp. 12401–12430.
- [60] P. Tong, E. Brown, P. Wu, S. Woo, A. J. V. IYER, S. C. Akula, S. Yang, J. Yang, M. Middepogu, Z. Wang *et al.*, "Cambrian-1: A fully open, vision-centric exploration of multimodal llms," *Proc. Adv. Neural Inf. Process. Syst.*, vol. 37, pp. 87310–87356, 2024.
- [61] H. Liu, C. Li, Y. Li, and Y. J. Lee, "Improved baselines with visual instruction tuning," in *Proc. IEEE Conf. Comput. Vis. Pattern Recognit.*, 2024, pp. 26296–26306.
- [62] G. Ilharco, M. Wortsman, R. Wightman, C. Gordon, N. Carlini, R. Taori, A. Dave, V. Shankar, H. Namkoong, J. Miller, H. Hajishirzi, A. Farhadi, and L. Schmidt, "Openclip," Jul. 2021, 0.1. [Online]. Available: https://github.com/mlfoundations/open_clip
- [63] S. Y. Gadre, G. Ilharco, A. Fang, J. Hayase, G. Smyrnis, T. Nguyen, R. Marten, M. Wortsman, D. Ghosh, J. Zhang *et al.*, "Datacomp: In search of the next generation of multimodal datasets," in *Proc. Adv. Neural Inf. Process. Syst.*, vol. 36, 2024.
- [64] H. Salman, A. Ilyas, L. Engstrom, A. Kapoor, and A. Madry, "Do adversarially robust imagenet models transfer better?" in *Proc. Adv. Neural Inf. Process. Syst.*, vol. 33, 2020, pp. 3533–3545.
- [65] W. Xu, D. Evans, and Y. Qi, "Feature squeezing: Detecting adversarial examples in deep neural networks," in *NDDS Symp.*, 2018.
- [66] M. Naseer, S. Khan, M. Hayat, F. S. Khan, and F. Porikli, "A self-supervised approach for adversarial robustness," in *Proc. IEEE Conf. Comput. Vis. Pattern Recognit.*, 2020, pp. 262–271.
- [67] W. Nie, B. Guo, Y. Huang, C. Xiao, A. Vahdat, and A. Anandkumar, "Diffusion models for adversarial purification," in *Proc. Int. Conf. Mach. Learn.*, 2022, pp. 16805–16827.